Biomechanics and Modeling in Mechanobiology
https://doi.org/10.1007/s10237-018-1105-9

ORIGINAL PAPER

GAG content, fiber stiffness, and fiber angle affect swelling-based residual stress in the intact annulus fibrosus

Bo Yang[1] · **Grace D. O'Connell**[1,2]

Received: 8 August 2018 / Accepted: 29 November 2018

Abstract
Biological tissues with a high glycosaminoglycan (GAG) content have an excellent ability to swell by absorbing water molecules from the surrounding environment. Our recent work showed that anisotropy in tissue swelling depends on the fiber-network architecture, including fiber angle, fiber stiffness, and lamellae structure. However, that work did not evaluate the effect of in situ boundary conditions, such as the kidney-bean shape of the annulus fibrosus (AF), on swelling behavior. The biochemical composition of intact AF is inhomogeneous with respect to GAG composition, collagen fiber angle, and fiber stiffness. Moreover, the GAG content in the inner AF decreases significantly with degeneration. In this study, we investigated the role of GAG content, fiber angle, and fiber stiffness in AF swelling and residual strain development using a finite element model based on a human lumbar disk. Our results showed that the annular ring structure had a great impact on swelling by developing region-dependent compressive stress/stretch in the inner layers and tensile stress/stretch in the outer AF. Swelling-based residual stretch was comparable to experimentally measured values, suggesting an important role of tissue swelling in maintaining residual stresses. Moreover, GAG loss in the inner AF, as observed with degeneration, decreased circumferential-direction stress by over 65%. Homogeneous distributions of fiber angle and stiffness overestimated or underestimated AF swelling behavior, such as swelling ratio, circumferential/axial stretch, and fiber stretch/reorientation. These findings demonstrate the need to include native fiber architecture in finite element models, to accurately predict tissue failure, as well as to cultivate engineered disks.

Keywords Swelling · Residual stress · Residual strain · Annulus fibrosus · Intervertebral disk · Fiber angle · Degeneration

1 Introduction

Many native and engineered fiber-reinforced tissues, such as the annulus fibrosus (AF) and arterial walls, have an excellent capacity to absorb water molecules from the surrounding environment (> 50% increase in volume) (Bezci and O'connell 2018; Fung 1991). Water uptake is directly related to the glycosaminoglycans (GAG) composition, and tissue deformations due to swelling lead to development of residual stresses and strains, altering tissue- and joint-level mechanics (Ateshian et al. 2009; Azeloglu et al. 2008; Bezci et al. 2015; Bezci and O'connell 2018; Emanuel et al. 2018; Fung 1991; Screen et al. 2006; Skaggs et al. 1994; Vergroesen et al. 2016; Żak and Pezowicz 2016). Previous experimental and computational studies have shown that tissue-swelling behavior of fiber-reinforced materials is anisotropic and dependent on the fiber-network architecture (i.e., fiber angle, lamellae, and fiber stiffness) (Yang and O'Connell 2018; Żak and Pezowicz 2016). Tissue swelling occurs as a balance between fiber deformation, fiber rotation, and matrix swelling (Demirkoparan and Pence 2018; Yang and O'Connell 2018). However, the effect of complex tissue geometry, such as the kidney-bean shape of the intervertebral disk, on swelling behavior and residual stress formation is not clear.

Recent work showed that the inner AF experiences large region-dependent compressive residual strains, while the outer AF experiences region-dependent tensile residual strains (Duclos and Michalek 2017; Mengoni et al. 2017; Michalek et al. 2012). Similar residual strain distribution, i.e., compressive in the inner region and tensile in the outer

✉ Grace D. O'Connell
g.oconnell@berkeley.edu

[1] Department of Mechanical Engineering, University of California, Berkeley, 5122 Etcheverry Hall, #1740, Berkeley, CA 94720, USA

[2] Department of Orthopaedic Surgery, University of California, San Francisco, San Francisco, USA

Published online: 10 December 2018

region, has also been observed in cardiovascular tissues (Fung 1991). In addition, residual strains in arterial wall depend on tissue composition and spatial location (i.e., through the wall thickness and distance from the heart) (Chuong and Fung 1986; Fung 1991). Comparisons can be made between the intervertebral disk and the arterial wall and, in that the healthy nucleus pulposus (NP) acts to pressurize the inner AF during loading. It is thought that residual stresses in the arterial wall act together with blood pressure to maintain a uniform stress distribution throughout the arterial wall (Rachev and Greenwald 2003). More recent work has shown that stress homeostasis through the arterial wall greatly depended on local GAG composition (Roccabianca et al. 2014). Interestingly, work by Roccabianca et al. showed that an increase in GAGs confined to a small region of the arterial wall increased radial stresses and strains that may cause arterial wall delamination (Roccabianca et al. 2014).

The biochemical composition of the AF is inhomogeneous from outer to inner with respect to GAG content, collagen fiber angle, and fiber stiffness. In non-degenerate disks, the GAG content increases from $3.0 \pm 0.3\%$ per wet weight in the outer AF to $8.0 \pm 0.5\%$ per wet weight in the inner AF (Antoniou et al. 1996; Urban and Maroudas 1979). Age and degeneration are noted by a ~60% decrease in GAG composition in the inner AF, while the GAG content in the outer AF remains relatively constant (Antoniou et al. 1996). Fiber angle, with respect to the transverse plane, increases from $\pm 28°$ in the outer AF to $\pm 43°$ in the inner AF (Cassidy et al. 1989). Lastly, collagen fibers in the outer AF are 2–3X stiffer than fibers in the inner AF, due to differences in collagen type and content (i.e., higher ratio of collagen type I:II in the outer AF) (Ebara et al. 1996; Eyre and Muir 1976; Holzapfel et al. 2005; Skaggs et al. 1994). Fiber stiffness is thought not to change greatly with degeneration (Acaroglu et al. 1995). Although there are large spatial variations in GAG content, fiber angle, and fiber stiffness, the role of these properties in AF swelling and residual strain development is not well understood.

Computational models are widely used to better understand stress distributions between tissues in the spine and to assess the role of degeneration in disk joint mechanics (Jacobs et al. 2014; Rohlmann et al. 2006; Schmidt et al. 2007). Many of these previous models described the AF using hyperelastic material descriptions, which are not capable of describing swelling behavior under various aqueous solutions observed in vivo. Moreover, these models described the AF as having a homogeneous fiber angle ($\pm 30°$) and stiffness (Marchand and Ahmed 1990; Shirazi-Adl et al. 1986; Yang and O'Connell 2017). Similarly, tissue-engineered strategies commonly use homogenized fiber stiffness and/or angle (either $0°$ or $\pm 30°$) to create de novo intervertebral disks (Bowles et al. 2010; Gullbrand et al. 2018; Martin et al. 2017; Nerurkar et al. 2010).

Our previous work evaluated the effect of the collagen fiber network on tissue-level swelling, where specimen geometry was based on the rectangular geometry commonly used for uniaxial testing (Yang and O'Connell 2018). However, in situ AF swelling will be affected by boundary conditions due to the kidney-bean geometry of the human disk. Therefore, the first objective of this study was to evaluate the effect of the kidney-bean geometry on the swelling behavior of the AF. The second objective was to evaluate residual strain formation as a result of swelling. Finally, we evaluated the effect of GAG content, fiber angle, and fiber stiffness on swelling and residual strain formation.

2 Methods

We developed two series of models (Table 1). Models in Series I contained 1 to 4 annular layers and were used to evaluate the effect of the kidney-bean geometry on annular ring swelling (Fig. 1a). The thin annular ring structures allowed us to compare annular ring results to our previous swelling results on rectangular specimens (Yang and O'Connell 2018). In addition, we included a 20-layer rectangular model to compare to the full AF annular ring model,

Table 1 Series I evaluated the effect of annulus ring (AR) geometry on bulk tissue swelling of single- and multi-lamellae structures

	Model	Total # of layers
Series I	1AR	1
	2AR	2
	3AR	3
	4AR	4
	20AR	20
	20REC	20
Series II	G-A-S (*Control*)	20
	HG-A-S	20
	G-HA-S	20
	HG-HA-S	20
	G-A-HS	20
	HG-A-HS	20
	G-HA-HS	20
	HG-HA-HS	20

A 20-layer rectangular (20REC) specimen was added to our previous simulations for comparison (Yang and O'Connell 2018). Series II investigated the effect of GAG distribution (G), fiber angle (A), and fiber stiffness (S) on AF swelling behavior. An H in front of G, A, or S represents a homogeneous distribution of the material property, where the default condition was an inhomogeneous distribution that represented native tissue architecture. HG-HA-HS model in Series II was the same as the 20AR model in Series I

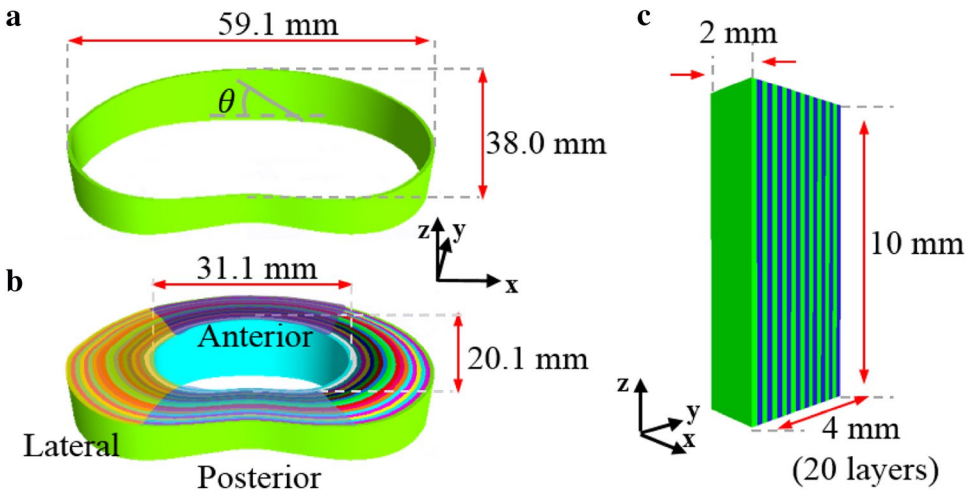

Fig. 1 **a** Representative model of annular rings (1 layer shown). **b** Complete AF model with 20 layers shared the same anterior–posterior width and lateral width as the 1-layer model. Anterior, posterior, and lateral regions are marked by transparent purple, yellow, and blue. **c** Rectangular model with 20 layers

which represented the native architecture of healthy human disks (Fig. 1b, c) (Marchand and Ahmed 1990). Models in Series II were all 20-layer annular ring models to represent the native AF (Fig. 1b). However, material properties in Series II models were modified to evaluate the role of inhomogeneous GAG composition, fiber angle, and fiber stiffness. In the Control model used for Series II, spatial distributions of GAG, fiber angle, and fiber stiffness through the annulus wall thickness were inhomogeneous and selected based on properties of healthy non-degenerate human lumbar disks reported in the literature (Antoniou et al. 1996; Cassidy et al. 1989; Holzapfel et al. 2005; Urban and Maroudas 1979; Yang and O'Connell 2017). In Series II, these parameters were modified to create a homogeneous distribution (denoted by H in front of the properties, Table 1), by changing the material properties in the inner AF to match the values in the outer AF ($n=8$ models; Table 1).

2.1 Model geometry and mesh

The model geometry and mesh were extracted from our previous joint-level model (Figs. 1a, b) (Yang and O'Connell 2017). Briefly, AF geometry and meshes were generated using a custom-written algorithm to process published data containing averaged disk geometry from human male L3-L4 disks ($n=13$; MATLAB 2013, Mathworks, Inc. Natick, MA) (Peloquin et al. 2014). In Series I models, annular rings were created by starting at the outermost layer (Fig. 1a) and building inward for multilayered models. The 20-layer rectangular model had same layer length, width, and thickness as our previous study (Yang and O'Connell 2018). Fibers were orientated at ±30° with respect to the transverse plane for annular ring models and with respect to Z-axis for the 20-layer rectangular model (Fig. 1c). Models in Series II contained AF geometry of the complete annulus fibrosus (20 layers), representing the native AF architecture (Fig. 1b). The fiber angle in Series II models was defined as either homogeneous (±30°) or inhomogeneous, ranging from ±43° in the innermost AF layer and decreasing linearly to ±28° in the outermost AF layer (Cassidy et al. 1989).

2.2 Material properties

Triphasic mixture theory was used to describe the tissue as a combination of three phases: a solid phase and two fluid phases (water and monovalent ions) (Ateshian et al. 2004; Lai et al. 1991; Maas et al. 2012). The solid phase consisted of the extrafibrillar matrix and nonlinear fibers, where W_i represents strain energy density functions (Eq. 1) (Maas et al. 2012). The extrafibrillar matrix was defined as a compressible hyperelastic material using the Holmes–Mow description (Eqs. 2–4). Matrix material properties were assumed to be spatially uniform and held consistent across all models. Material coefficients (E_m, ν, and β) were selected based on values reported in the literature (Table 2) (Cortes et al. 2014). E_m, ν, and β represent Young's modulus, Poisson's ratio, and material exponential stiffening coefficient, respectively.

$$W = W_{\text{matrix}} + W_{\text{fiber}} \tag{1}$$

$$W_{\text{matrix}}(I_1, I_2, J) = \frac{1}{2}c\left(e^{Q} - 1\right) \tag{2}$$

where Q and c were expressed as:

$$Q = \frac{\beta}{\lambda + 2\mu}\left[(2\mu - \lambda)(I_1 - 3) + \lambda(I_2 - 3) - (\lambda + 2\mu)lnJ^2\right] \tag{3}$$

$$c = \frac{\lambda + 2\mu}{2\beta} \tag{4}$$

I_1 and I_2 are the first and second invariants of the right Cauchy–Green deformation tensor, $\mathbf{C}$ ($\mathbf{C}=\mathbf{F}^{\mathrm{T}}\mathbf{F}$) and J

Table 2 Material parameters for models in Series I

Solid phase		Fluid phase	
E_m (MPa)	0.025	k_0 $\left(\text{mm}^4/(\text{Ns})\right)$	0.0064
υ (unitless)	0.16	M (unitless)	4.8
β (unitless)	3.3	ϕ (unitless)	0.938
E_f (MPa)	46	FCD (mmol/L)	− 100
γ (unitless)	4.5	D_{free} $\left(\text{mm}^2/\text{s}\right)$	0.00147
I_0 (unitless)	1.06	D $\left(\text{mm}^2/\text{s}\right)$	0.0008
φ_0 (unitless)	0.3	S (unitless)	1

E_m, Extrafibrillar matrix modulus; υ, Poisson ratio; β, nonlinear parameter for the Holmes–Mow description; E_f, collagen fiber modulus; γ, exponential term for the toe-region response of the fibers; I_0, the stretch ratio between the toe- and linear-regions; φ_0, tissue solid fraction; k_0, hydraulic permeability in the reference configuration; M, nonlinear parameter for permeability; ϕ, osmotic coefficient; FCD, fixed charge density; D_{free}, ion diffusivity in water; D, ion diffusivity within tissue; and S, ion solubility (Cortes et al. 2014; Holzapfel et al. 2005; Urban and Maroudas 1979; Yang and O'Connell 2017)

are the Jacobian of the deformation gradient tensor, **F** ($J = \det(\mathbf{F})$). λ and μ are the Lamé coefficients, which are related to Young's modulus (E_m) and Poisson's ratio (ν).

Fibers were defined using a nonlinear stress–stretch relationship with defined toe- and linear-regions separated by a transition stretch value (λ_0, $I_0 = \lambda_0^2$, Eqs. 5–8) (O'Connell et al. 2009). In Eq. 5, Υ describes the toe-region nonlinearity (unitless), the invariant I_n represents the square of the fiber stretch ($I_n = \mathbf{a}\cdot\mathbf{C}\cdot\mathbf{a}$, where **a** is the unit vector that describes the fiber angle in the reference configuration), and E_f represents the fiber linear-region elastic modulus (MPa, constant). In this expression, Υ, I_0, and E_f are independent coefficients, which were calibrated using data from single-lamellae tensile tests (Holzapfel et al. 2005), as described previously (Yang and O'Connell 2017). Fiber stiffness in Series I models was homogeneous and calibrated to the stiffness of single-lamellae from the outer AF (Table 2). The fiber stiffness in Series II models was either held constant throughout the AF or inhomogeneous, increasing linearly from the inner AF to outer AF (Table 3). All fibers were limited to acting only in tension.

$$W_{\text{fiber}} = \begin{cases} 0 & I_n < 1 \\ \frac{\xi}{2\gamma}\left(I_n - 1\right)^{\gamma} & 1 \le I_n \le I_0 \\ E_f\left(I_0^{\frac{1}{2}} - I_n^{\frac{1}{2}}\right) + B\left(I_n - I_0\right) + W_0 & I_0 \le I_n \end{cases} \tag{5}$$

$$\xi = \frac{E_f}{2(\gamma - 1)} I_0^{-3/2}\left(I_0 - 1\right)^{2-\gamma} \tag{6}$$

$$B = \frac{E_f I_0^{-3/2}}{2}\left[\frac{I_0 - 1}{2(\gamma - 1)} + I_0\right] \tag{7}$$

Table 3 Additional material parameters for models in Series II (other parameters are shown in Table 2)

	Inhomogeneous		Homogeneous
	Inner AF	Outer AF	
FCD (mmol/L)	− 300	− 100	− 100
Fiber angle	43°	28°	30°
Fiber stiffness			
E_f (MPa)	16.5	46	46
γ (unitless)	5.5	4.5	4.5
I_0 (unitless)	1.09	1.06	1.06

For inhomogeneous model descriptions values were linearly interpolated from the inner AF to the outer AF. E_f, collagen fiber modulus; γ, exponential term for the toe-region response of the fibers; I_0, the stretch ratio between the toe- and linear-regions; FCD, fixed charge density (Antoniou et al. 1996; Cassidy et al. 1989; Holzapfel et al. 2005; Urban and Maroudas 1979; Yang and O'Connell 2017)

$$W_0 = \frac{\xi}{2\gamma}\left(I_0 - 1\right)^{\gamma} \tag{8}$$

In the triphasic mixture theory, the negative fixed charge density (FCD) in the solid description was used to represent the GAG composition in the extrafibrillar matrix by assuming 2 mol of charge per GAG mole (molecular weight = 502.5 g/mol; Eq. 9) (Jackson et al. 2009). An FCD of − 100 mmol/L was used for annular rings in Series I, representing the GAG content in the outer AF (Urban and Maroudas 1979). Similar to fiber angle and stiffness, the GAG distribution of models in Series II was either held fixed at − 100 mmol/L or was inhomogeneous, decreasing linearly from − 300 mmol/L in the inner AF to − 100 mmol/L in the outer (Table 3) (Antoniou et al. 1996; Urban and Maroudas 1979). The total number of fixed charges was conserved; therefore, the local FCD depended on volumetric changes (Eq. 10; φ_0 represents the solid volume fraction in the reference configuration, subscript '0' for FCD represents the reference configuration, while '1' represents the swollen configuration; Table 2).

$$\text{FCD}_0 = \frac{2\ \text{mmol charges}}{0.5025\ \text{g GAG}} \frac{W_{\text{GAG}}}{1\ \text{L}} \tag{9}$$

$$\text{FCD}_1 = \frac{1 - \varphi_0}{J - \varphi_0}\text{FCD}_0 \tag{10}$$

Fluid (i.e., water) and ion phases were included to simulate tissue swelling (Table 2) (Stadie and Sunderman 1931; Yasuda et al. 1968). FCD influenced fluid and ions movement by affecting their electrochemical potential. Free diffusivity (D_{free}) and diffusivity (D) were used to describe how quickly ions diffused through the water and the tissue. Permeability (k) was used to describe fluid flow through the

tissue and was strain dependent. Parameters k_0 and M were selected based on AF experimental data (Holmes–Mow permeability model; Eq. 11; Table 2) (Cortes et al. 2014).

$$k(J) = k_0 \left(\frac{J - \phi_0}{1 - \phi_0} \right)^2 e^{1/2M(J^2-1)} \tag{11}$$

2.3 Simulation, model validation, and data analyses

All simulations were conducted in FEBio (Maas et al. 2012). Boundary conditions for all models allowed specimens to freely deform, except that bulk tissue translational movement was restricted. This was achieved by fixing one degree of freedom of a few nodes such that the X-position was fixed for three nodes on the bottom and mid-sagittal planes (YZ plane), the Y-position was fixed for three nodes on the bottom and anterior region, and the Z-position was fixed for six nodes on the mid-transverse plane (XY plane). These nodes were picked to utilize AF swelling symmetry. The reference configuration represented a state of osmotic dehydration, which is equivalent to the tissue hydrated under an infinitely high concentration of saline. Steady-state swelling (quasi-static) condition was simulated by increasing the FCD from zero to the specified value (10 steps in 1-s simulation), while the saline condition of the surrounding environment remained constant (0.15 M phosphate-buffered saline; 150 mmol/L). Since the simulation was quasi-static, water and ion redistribution and tissue deformation reached equilibrium at each time-step.

Deformations caused by free-swelling conditions were analyzed. The swelling ratio was calculated as the volume in the deformed condition divided by the volume in the reference configuration. Swelling ratio, fiber stretch, and fiber reorientation were calculated for each element. Weighted averages were calculated for each parameter, using element volumes as a weighting factor. For complete AF ring models (20 layers), circumferential, axial, and radial stretch and stress were calculated for each element. Weighted averages were calculated for each layer, as well as for the whole model, to calculate layer-averaged and model-averaged values. It should be noted that circumferential and radial directions referred to local coordinates (i.e., normal to and aligned with the lamellae, respectively). Lastly, region-dependent swelling was evaluated for the anterior, lateral, and posterior regions of the innermost and outermost layers (Fig. 1b). Only fibers in tension were included in the calculation of average fiber stretch.

In our previous study, rectangular models that represented samples used in uniaxial tensile tests were validated by comparing volumetric and dimensional changes from swelling to free-swelling experiments on bovine AF explants (Bezci et al. 2015; Yang and O'Connell 2018; Żak and Pezowicz 2016). In the current study, annular rings in Series I used the same material properties and fiber angle. Further validation was performed for the Control model in Series II. The circumferential-direction stretch was compared with experimentally measured residual stretches of bovine disks (Duclos and Michalek 2017; Michalek et al. 2012). The Control model was considered valid if the circumferential stretch in inner and outer AF followed the same behavior of experimental observations and the magnitude was within one standard deviation of the reported mean.

3 Results

3.1 Model validation

The volume of the Control AF model increased by 58% under free-swelling conditions, which was comparable to values reported in the literature (up to 70%) (Bezci et al. 2015; Żak and Pezowicz 2016). Swelling of the Control AF model resulted in compressive circumferential stretch in the innermost AF layer (layer-averaged stretch = 0.92) and tensile circumferential stretch in the outermost AF layer (stretch = 1.076), which was within one standard deviation of the residual stretch measured in bovine AF explants (Fig. 2) (Duclos and Michalek 2017; Michalek et al. 2012). Since model results were comparable to reported values, the Control AF model was considered valid for evaluating AF swelling behavior.

3.2 Effect of annular rings (Series I)

In general, within 1–4 layers, annular ring models had a similar response to ± 30° rectangular models with respect to swelling ratio, fiber stretch, and fiber reorientation. For the 1-layer annular ring model, there was a 52% increase in volume with swelling (swelling ratio = 1.52; Fig. 3a,

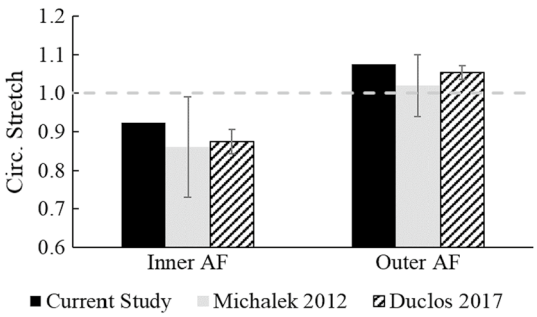

Fig. 2 Circumferential stretch due to osmotic swelling in the inner and outer AF for the Control model was within one standard deviation of the reported mean in the literature (Duclos and Michalek 2017; Michalek et al. 2012). Gray dashed line represents a stretch-free condition

b), resulting in an average tensile fiber stretch of 1.019 and fiber reorientation of ~ 5°. Annular ring models with 2–4 layers had a decrease in lateral width and an increase in anterior–posterior width with swelling, making the specimens slightly more rounded (Fig. 3a—2nd row). The 2-layer annular ring model experienced twisting, which was similar to observations for even-layered rectangular specimens; however, twisting was not observed in annular ring specimens with four or more layers (Fig. 3a). The largest difference in swelling ratio between rectangular and annular ring specimens was observed with 2- and 20-layer models, where the kidney-bean geometry resulted in less tissue swelling (swelling ratio for 20-layer models = 1.45 for rectangular vs. 1.41 for the annular ring; Fig. 3b).

There were large differences in the swelling behavior of the 20-layer annular ring model when compared to the 20-layer rectangular model. Swelling with a kidney-bean geometry resulted in the formation of inhomogeneous stretch and stress in the circumferential direction. The circumferential-direction stretch and stress were compressive in the inner layers and tensile in the outer layers (Fig. 3c, d).

3.3 Complete AF model (Series II)

Swelling caused dimensional changes for all 8 models in Series II. The anterior–posterior width of the outer AF increased by 19% in the HG-HA-HS model (i.e., homogeneous description) and 31% in the G-A-S model (i.e., spatial variation in properties). In contrast, the lateral width of the outer AF was relatively consistent with swelling (< 3% change from reference configuration), making the final specimen geometry slightly more circular after swelling (Figs. 4, 5—1st row). The anterior–posterior width of the inner AF also increased with swelling; however, the lateral width of the inner AF experienced contraction (Figs. 4, 5—2nd row).

The average swelling ratio was between 1.41 (HG-HA-HS) and 1.61 (G-HA-S; Figs. 4, 5—1st row). The swelling ratio of models with an inhomogeneous GAG distribution (1.53–1.61) was greater than the swelling ratio of models with a homogeneous GAG distribution (1.41–1.44). The

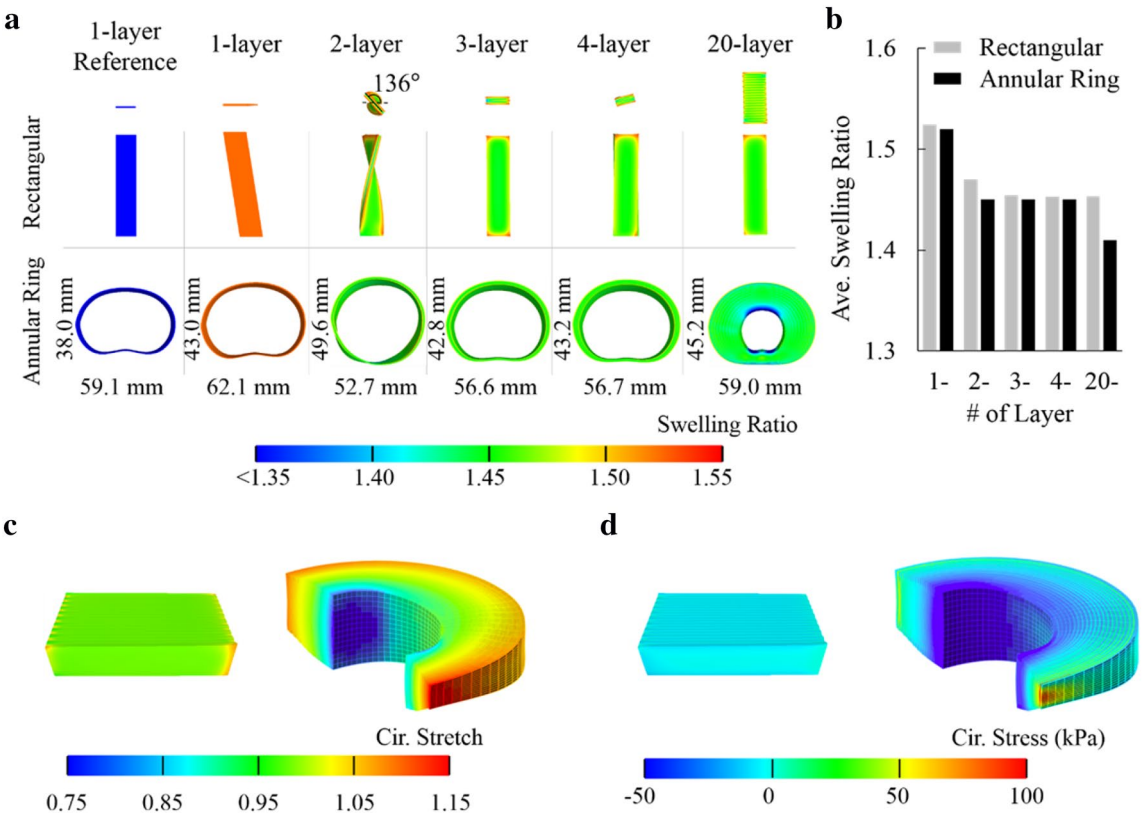

Fig. 3 **a** Swelling and bulk deformations of rectangular models and annular ring models. Images for 1–4 layer rectangular specimens adapted from Yang and O'Connell (2018). **b** Model-averaged swelling ratio for rectangular and annular ring models. **c** Longitudinal stretch (Z-axis) in the 20-layer rectangular model and circumferential-direction stretch in the 20-layer annular ring model (full AF model) after swelling. **d** Longitudinal stress (Z-axis) in the 20-layer rectangular model and circumferential stress in the 20-layer annular ring model after swelling

swelling ratio was higher in the lateral AF than in the anterior and posterior AF, regardless of the spatial distribution of GAGs, fiber angle, or fiber stiffness (Fig. 6a, b). Homogeneous distribution of GAGs (HG) throughout the AF reduced swelling in the inner AF by ~50% (Fig. 7-blue lines vs. black lines). Swelling of the inner AF was also decreased by a homogeneous distribution of fiber stiffness (HS; Fig. 7—triangles vs. circles), but increased by a homogeneous fiber angle (HA; Fig. 7—dashed line vs. solid line).

Along the circumferential direction, all models developed compressive stretch and stress in the inner AF and tensile stretch and stress in the outer AF (Figs. 4, 5—2nd and 3rd rows). Region-based differences showed that the compressive stresses in the inner AF were highest in the anterior AF and lowest in the lateral AF (Fig. 6c—black bars). Tensile stresses in the outer AF were highest in the posterior AF and were 2–3.5X greater than the tensile stresses in the anterior and lateral AF (Fig. 6d—black bars). A homogenous GAG distribution decreased stresses in the inner and outer AF of all three regions by over 60%, with the largest absolute drop observed in the anterior inner AF and the posterior outer AF (Fig. 7c, d—black bar vs. gray bar). Layer-averaged circumferential-direction stress also highlighted the decrease in stress with a homogenous description of GAGs (Fig. 8b—blue vs. black lines). Using a homogeneous fiber angle (HA) or fiber stiffness (HS) description had a relatively little impact on region-dependent circumferential-direction stress, except for the tensile stresses in the outer posterior AF (Fig. 6d—black bar vs. patterned bars).

A homogeneous distribution of GAGs (HG) had little impact on the circumferential-direction stretch in the inner AF, but caused a 50% decrease in the circumferential-direction tensile stretch in the outer AF (Fig. 8a—blue vs. black lines). Homogeneous fiber stiffness (HS) increased the circumferential-direction compressive stretch at the inner AF by more than 50%, but had a relatively little impact on the circumferential-direction stretch in the outer AF (Fig. 8a—triangles vs. circles). A homogeneous distribution of fiber angle (HA) had a relatively small effect on the stretch in the circumferential direction (Fig. 8a—dashed vs. solid lines).

In general, all models developed tensile stretch in the axial direction of the inner AF, (Figs. 4, 5—4th row). In the Control model, the tensile stretch was 1.27 in the inner AF and the magnitude decreased linearly from the inner AF to the outer AF such that the axial-direction stretch was compressive in the outer AF (Figs. 4, 5—4th row). A homogeneous distribution of GAGs and fiber stiffness (HG and HS) resulted in relatively uniform axial-direction stretch throughout the AF. That is, there was a 30% decrease in axial-direction stretch from the inner AF to the outer AF in the G-HA-S model, but only decreased by 8% in the HG-A-HS model (Fig. 8c—blue vs. black lines). The axial-direction tensile stress in the inner AF decreased with a homogeneous distribution of GAGs or fiber stiffness (HG and HS; Fig. 8c—blue vs. black lines or triangles vs. circles) and increased with a homogeneous distribution of fiber angle (HA; Fig. 8c—solid vs. dashed lines). Axial-direction stress was relatively low in all models, save for the innermost and outermost layers, which experienced tensile and compressive stresses, respectively (Figs. 4, 5—5th row—and 8d).

Large tensile deformations were observed in the radial direction, with the lowest values observed in the posterior–lateral AF (Figs. 4, 5—6th row). Layer-averaged radial stretches greater than 1.2, with values near 1.3 in the outer AF for all models (Fig. 8e). Layer-averaged radial stretch was higher in the inner AF than in the outer AF of models with an inhomogeneous GAG distribution, while the layer-averaged radial stretch was relatively consistent throughout the AF in models with a homogeneous GAG distribution (HG; Fig. 8e—blue vs. black lines). Radial stretch decreased with a homogeneous distribution in fiber angle (HA; Fig. 8e—dashed vs. solid lines) and increased with a homogeneous distribution in fiber stiffness (HS; Fig. 8e—triangles vs. circles). Radial-direction stresses were relatively low throughout the AF ($\leq$ 13 kPa; Figs. 4, 5—7th row—and 8f). Layer-averaged radial stresses were slightly higher in the middle layers of the AF for models with inhomogeneous GAG distribution (Fig. 8f—blue vs. black lines).

Fiber stretch in the inner AF was lower in the anterior and posterior regions than in the lateral regions, but, in the outer AF, fiber stretch was highest in the anterior and posterior regions (Fig. 4, 5—8th row). All models had similar fiber stretch in the outermost layer (average = 1.03; Fig. 4, 5—8th row—9a). Fiber stretch was greatly reduced by a homogeneous distribution in fiber stiffness and GAG (HS & HG; Fig. 9a—triangles vs. circles and blue vs. black lines). Fiber stretch in the inner AF decreased with a homogeneous distribution of fiber angle (HA), but did not alter fiber stretch in the middle or outer AF (Fig. 9a—dashed vs. solid lines). The greatest layer-averaged fiber stretch occurred in the inner AF of the Control (G-A-S) model (1.10), and the lowest layer-averaged fiber stretch occurred in the inner AF of the homogeneous (HG-HA-HS) model (1.01; Fig. 9a—black solid line with circles vs. blue dashed line with triangular markers).

The behavior of fiber reorientation with swelling was similar for all models (Figs. 4, 5—last row). Fibers in the inner AF reoriented toward the axial direction (positive fiber reorientation; Figs. 4, 5—last row), while fibers in the anterior and posterior regions of the outer AF reoriented toward the transverse plane (Fig. 9b—black lines). A homogeneous distribution of GAGs (HG) decreased the magnitude of fiber reorientation throughout the AF (Fig. 9b—blue vs. black lines).

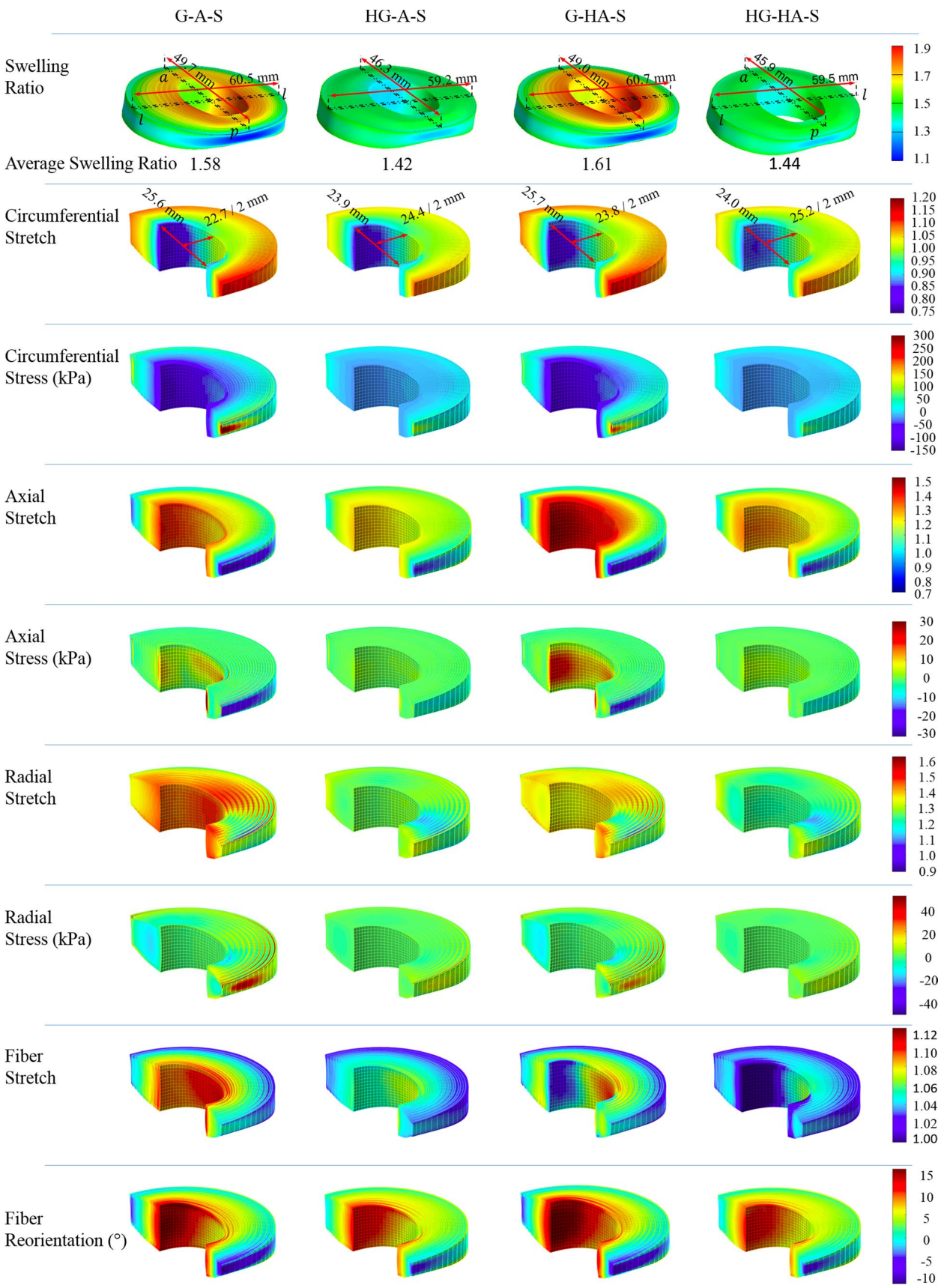
G-A-S
HG-A-S
G-HA-S
HG-HA-S
Swelling Ratio
49.7 mm
60.5 mm
46.3 mm
59.2 mm
49.0 mm
60.7 mm
45.9 mm
59.5 mm
a
l
p
1.9
1.7
1.5
1.3
1.1
Average Swelling Ratio 1.58
1.42
1.61
1.44
Circumferential Stretch
25.6 mm
22.7 / 2 mm
23.9 mm
24.4 / 2 mm
25.7 mm
23.8 / 2 mm
24.0 mm
25.2 / 2 mm
1.20
1.15
1.10
1.05
1.00
0.95
0.90
0.85
0.80
0.75
Circumferential Stress (kPa)
300
250
200
150
100
50
0
-50
-100
-150
Axial Stretch
1.5
1.4
1.3
1.2
1.1
1.0
0.9
0.8
0.7
Axial Stress (kPa)
30
20
10
0
-10
-20
-30
Radial Stretch
1.6
1.5
1.4
1.3
1.2
1.1
1.0
0.9
Radial Stress (kPa)
40
20
0
-20
-40
Fiber Stretch
1.12
1.10
1.08
1.06
1.04
1.02
1.00
Fiber Reorientation (°)
15
10
5
0
-5
-10

◂**Fig. 4** Swelling ratio, stretch and stress in the circumferential, axial, and radial directions, fiber stretch, and fiber reorientation. Data shown for G-A-S (Control model), HG-A-S, G-HA-S, and HG-HA-S models ($n=4/8$; data for the other models are shown in Fig. 5). In the last row, positive value represents fiber reorientation toward axial direction, while negative value represents fiber reorientation toward the transverse plane

4 Discussion

Simulations showed that the annular ring geometry for specimens with 4 or fewer layers had little impact on swelling ratio, fiber stretch, and fiber reorientation. However, the kidney-bean shape played an important role as the number of lamellae increased toward the native AF architecture (20 layers) such that circumferential-direction stretch and stress in the full AF model were compressive in the inner AF and tensile in the outer AF. These stretch and stress were comparable to experimental observations (Figs. 3, 4—2nd row) (Duclos and Michalek 2017; Michalek et al. 2012). Altering the distribution of GAGs, fiber stiffness, or fiber angle affected the magnitude and distribution AF swelling, stress and stretch, fiber reorientation, and fiber stretch.

Previous studies showed that residual strains of the bovine AF and arterial walls are compressive at the inner layers and tensile at the outer layers (Chuong and Fung 1986; Duclos and Michalek 2017; Fung 1991; Mengoni et al. 2017; Michalek et al. 2012). Inhomogeneous distributions of circumferential-direction stresses (compressive at the inner wall and tensile at the outer wall) are important to maintain a uniform tensile circumferential stress distribution throughout the wall during physiological loading (Rachev and Greenwald 2003). These findings suggest that AF residual stress is driven largely by the inner AF GAG content. This is further supported by the AF having a larger GAG content than other fiber-reinforced tissues that only experience tensile residual strains (e.g., 10–50 times higher GAG content than tendons or ligaments) (Amiel et al. 1983; Rigozzi et al. 2009).

Material properties in the full AF models were region independent, but residual stretch, residual stress, fiber stretch, and fiber reorientation were region dependent due to the asymmetrical AF geometry (Figs. 4, 5, 6). Larger compressive strains were predicted in the circumferential direction of the anterior inner AF, which agreed well with experimental observations. However, Duclos and Michalek reported tensile compressive strains in the posterior AF and regional differences that showed greatest tensile strains in the outer AF of the lateral AF, which did not agree well with our model predictions (Duclos and Michalek 2017). In both the bovine and human disks, peak tensile residual strains in the outer AF corresponded to areas with the smallest radius of curvature in the inner AF. Outer dimensions of the bovine disk are cylindrical, but the NP is more elliptical with the long axis along the lateral width (O'connell et al. 2007). Similarly, the kidney-bean shape of the human disk results in a lower radius of curvature in the posterior AF. The kidney-bean shape of human lumbar disks combined with layer-dependent material properties resulted in more complex distributions of residual stress and strain (Antoniou et al. 1996; Cassidy et al. 1989; Holzapfel et al. 2005; Skaggs et al. 1994).

In this study, GAG loss in the inner AF was described by a decrease in fixed charge density to match the fixed charge density of the outer AF. Diurnal loading causes a fluctuation in fluid volume by up to 20% (Botsford et al. 1994), altering disk joint stiffness (Bezci et al. 2015; Bezci and O'connell 2018; Emanuel et al. 2018; Vergroesen et al. 2016). Regardless of hydration condition, the swelling capacity of the healthy AF has been shown to be approximately 70% of the NP (Bezci et al. 2015). Therefore, AF swelling and residual strains likely fluctuate with the diurnal loading and hydration conditions.

The quantity and quality of GAGs in the inner AF decrease greatly with age and degeneration (Antoniou et al. 1996; Roughley et al. 2006; Urban and Maroudas 1979). We showed that GAG loss in the inner AF impacts swelling capacity, tissue deformations, and development of residual strains (Figs. 4, 5, 6, 7, 8—HG vs. G). Radial pressure from the NP, applied to a hydrated AF, would decrease the magnitude of stress and strain in the circumferential direction. Early degenerative changes are noted with a decrease in NP GAG content and intradiscal pressure (Adams and Roughley 2006). These changes, however, may increase the magnitude of compressive strains in the inner AF during physiological loading. Thus, it is likely that tissue remodeling in the inner AF occurs with age and degeneration to maintain stress homeostasis throughout the AF. The findings from this study support the notation that tissue remodeling through GAG deletion, rather than collagen stiffening, is more effective in reducing residual strains.

While the motivation for studying GAG distribution on residual strain formation in the AF was based on arterial wall research, there are interesting differences that should be noted. The GAG content in arterial walls increases due to an increase in blood pressure with disease (Roccabianca et al. 2014). Together, these findings support the notion that GAGs are crucial for maintaining stress homeostasis with disease and degeneration, especially in annular ring structures. Moreover, variations in local GAG composition may result in regional differences in circumferential strains that may increase the risk of annular tears (Duclos and Michalek 2017).

A decrease GAGs in the inner AF resulted in a reduction in the magnitude of axial-direction stretch and fiber reorientation (Figs. 8c, 9b). This finding is comparable to the decrease in fiber reorientation with degenerated AF tissue

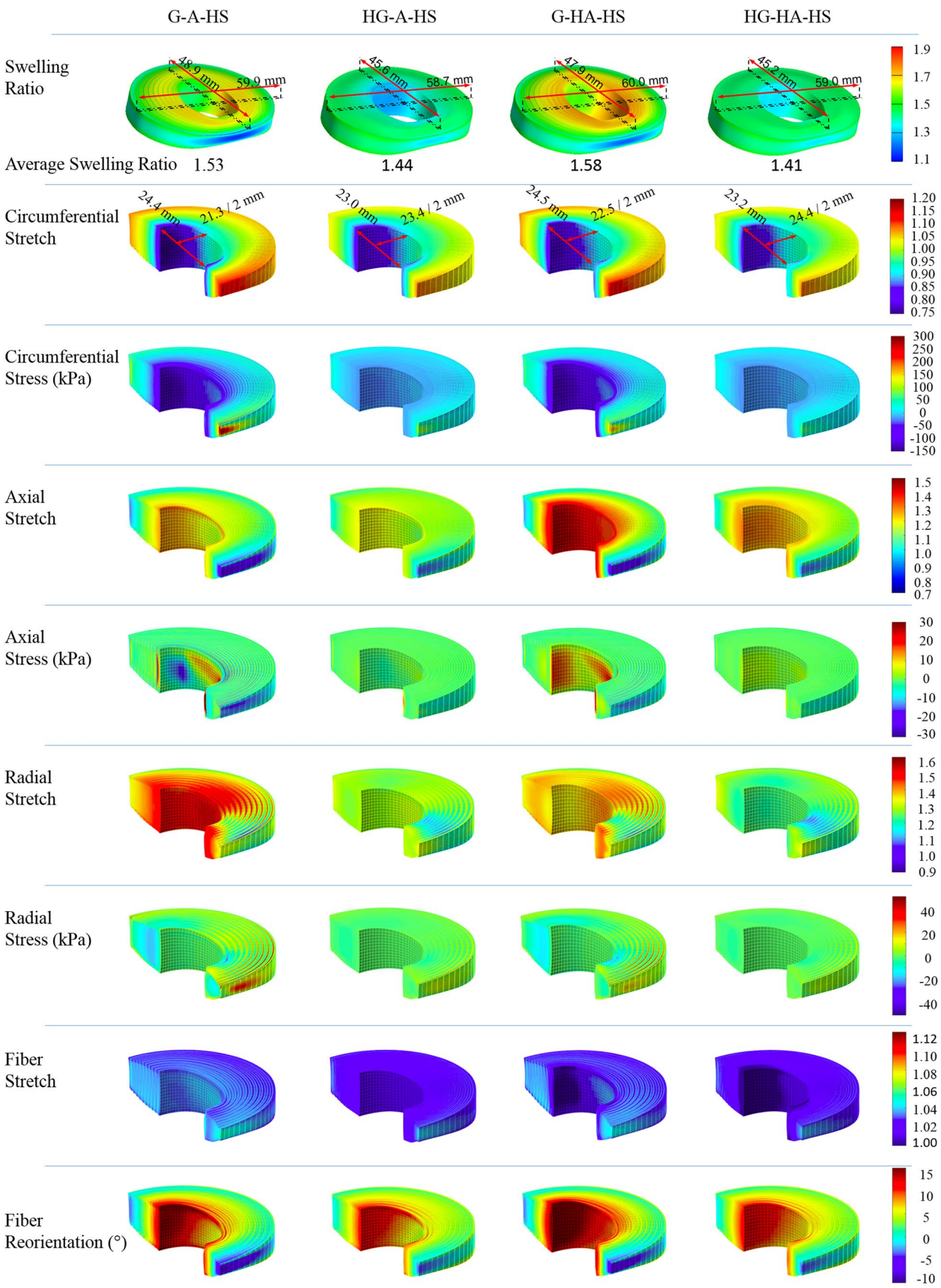
G-A-HS
HG-A-HS
G-HA-HS
HG-HA-HS
Swelling Ratio
48.9 mm
59.9 mm
45.6 mm
58.7 mm
47.9 mm
60.0 mm
45.2 mm
59.0 mm
1.9
1.7
1.5
1.3
1.1
Average Swelling Ratio 1.53
1.44
1.58
1.41
Circumferential Stretch
24.4 mm
21.3 / 2 mm
23.0 mm
23.4 / 2 mm
24.5 mm
22.5 / 2 mm
23.2 mm
24.4 / 2 mm
1.20
1.15
1.10
1.05
1.00
0.95
0.90
0.85
0.80
0.75
Circumferential Stress (kPa)
300
250
200
150
100
50
0
-50
-100
-150
Axial Stretch
1.5
1.4
1.3
1.2
1.1
1.0
0.9
0.8
0.7
Axial Stress (kPa)
30
20
10
0
-10
-20
-30
Radial Stretch
1.6
1.5
1.4
1.3
1.2
1.1
1.0
0.9
Radial Stress (kPa)
40
20
0
-20
-40
Fiber Stretch
1.12
1.10
1.08
1.06
1.04
1.02
1.00
Fiber Reorientation (°)
15
10
5
0
-5
-10

◂**Fig. 5** Swelling ratio, stretch and stress in the circumferential, axial, and radial directions, fiber stretch, and fiber reorientation. Data shown for G-A-HS, HG-A-HS, G-HA-HS, and HG-HA-HS models ($n=4/8$; data for the other models are shown in Fig. 4). In the last row, positive value represents fiber reorientation toward axial direction, while negative value represents fiber reorientation toward the transverse plane

under ex situ tensile loading (Guerin and Elliott 2006). Fiber reorientation in tissue-level specimens increases fiber engagement during tensile loading (Guerin and Elliott 2006). Moreover, changes in fiber orientation affect joint-level mechanics such that disks with fibers oriented closer to the axial plane have a higher torsional stiffness and larger shear strains at the AF–bone boundary (Yang and O'Connell 2017). Therefore, a decrease in fiber reorientation with GAG remodeling in the inner AF may help to protect the fibers from experiencing larger deformations during complex joint loading (e.g., compression with bending).

Our previous work showed that fiber orientation affected the swelling behavior of rectangular tissue specimens, while fiber stiffness only affected fiber stretch (Yang and O'Connell 2018). However, in the annular ring structure, both fiber orientation and fiber stiffness (HA & HG) altered swelling behavior. A homogeneous fiber angle (HA) description resulted in an overestimation of swelling ratio, axial stretch, and fiber reorientation, while predictions for radial stretch and fiber stretch were underestimated (G-A-S vs. G-HA-S model). A homogenous description of fiber stiffness (HS; i.e., an increase in inner AF fiber stiffness) decreased swelling ratio, stretch in the circumferential and axial directions, and fiber stretch (Figs. 7, 8, 9). A decrease in circumferential-direction residual stretch due to stiffer fibers may lead to an underestimation of deformations during mechanical loading. Taken together, these findings suggest that recapitulating spatial variations in fiber stiffness and fiber angle is important for properly describing AF mechanics and, therefore, joint-level mechanics.

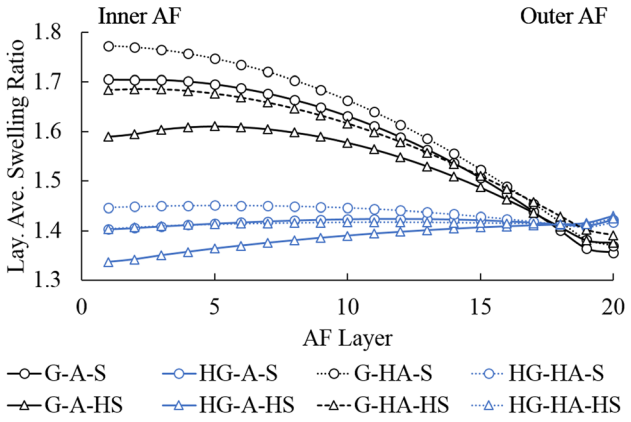

Fig. 7 Layer-averaged swelling ratio for each layer within an AF model (shown for all eight models in Series II). Black lines represent models with inhomogeneous GAG distribution (black for G), while blue lines represent models with a homogeneous distribution in GAG (blue for HG). Solid lines represent models with an inhomogeneous distribution in fiber angles, while dashed lines represent models with a homogeneous distribution in fiber angles. Circles represent models with an inhomogeneous distribution in fiber stiffness, while triangles represent models with a homogeneous distribution in fiber stiffness

Fig. 6 Swelling ratio averaged for the anterior, lateral, and posterior regions of innermost **a** and outermost **b** layers for G-A-S, HG-A-S, G-HA-S, and G-A-HS models. Compressive and tensile circumferential stress averaged for the anterior, lateral, and posterior regions of innermost **c** and outermost **d** layers for G-A-S, HG-A-S, G-HA-S, and G-A-HS models

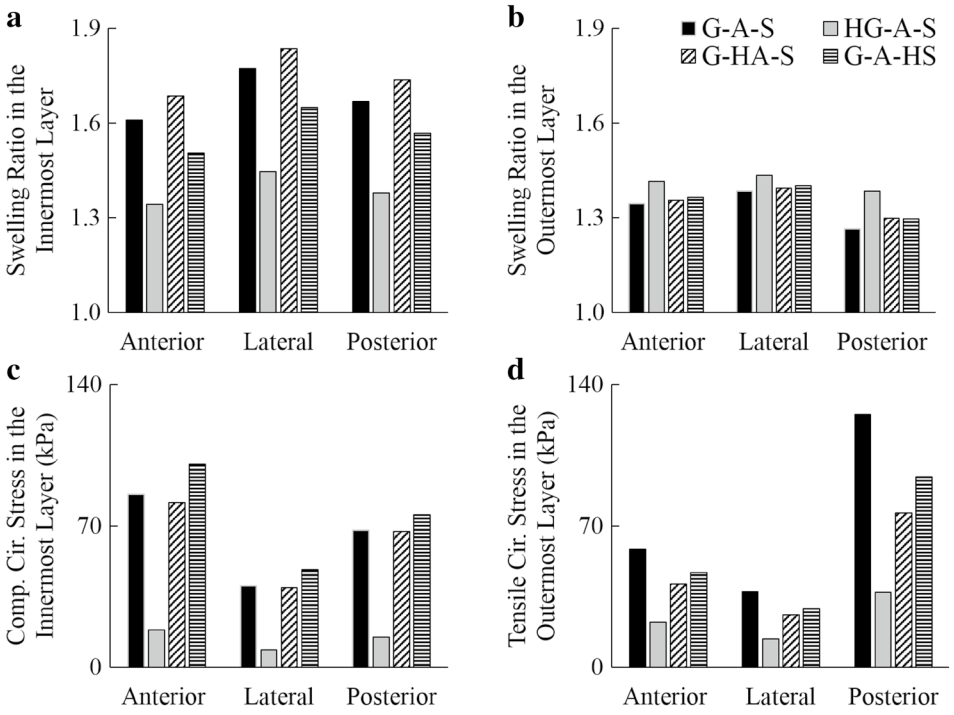

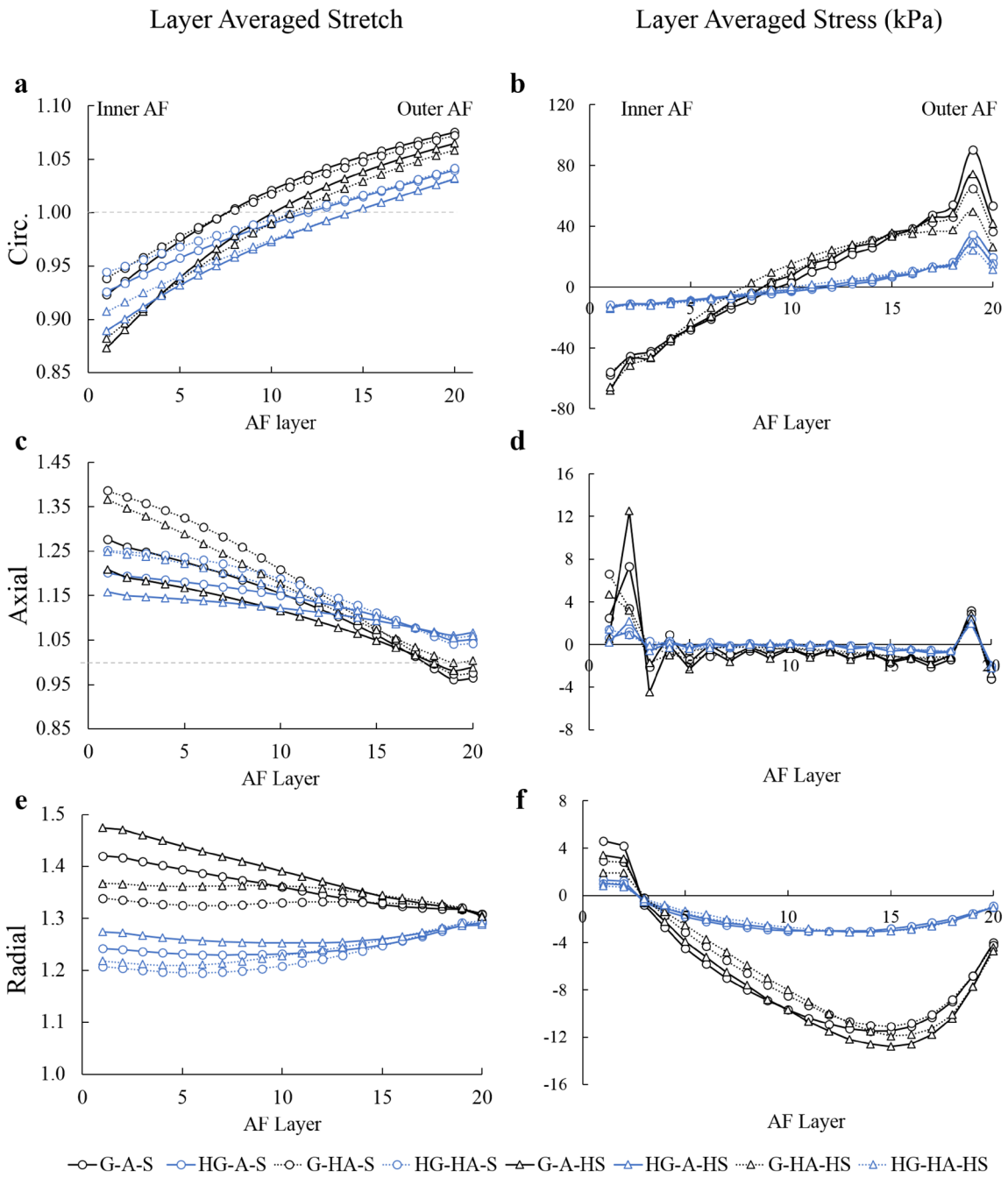

Fig. 8 Layer-averaged stretches and stresses for models in Series II. Layer-averaged **a** circumferential stretch, **b** circumferential stress, **c** axial stretch, **d** axial stress, **e** radial stretch, and **f** radial stress. Black lines represent models with inhomogeneous GAG distribution (black for G), while blue lines represent models with a homogeneous distribution in GAG (blue for HG). Solid lines represent models with an inhomogeneous distribution in fiber angles, while dashed lines represent models with a homogeneous distribution in fiber angles. Circles represent models with an inhomogeneous distribution in fiber stiffness, while triangles represent models with a homogeneous distribution in fiber stiffness

While the current model included spatial variations in GAG content, fiber stiffness, and fiber orientation, regional differences in fiber stiffness, fiber angle, and matrix composition were not investigated and may result in more complex strain distributions (i.e., differences between anterior and posterior AF) (Holzapfel et al. 2005; Skaggs et al. 1994) (Duclos and Michalek 2017). Due to a lack of experimental data, comparisons between model predictions and experimental data were limited to comparing results from bovine disks. The difference in disk geometry (kidney-bean shape

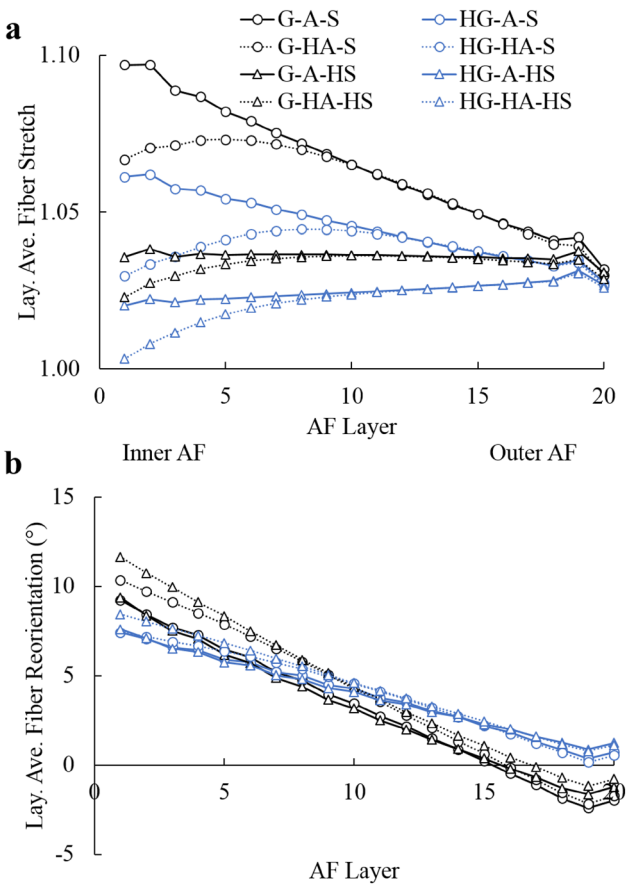

Fig. 9 Layer-averaged **a** fiber stretch and **b** fiber reorientation for each layer. Positive value represents fiber reorientation toward axial direction, while negative value represents fiber reorientation toward the transverse plane. Black lines represent models with inhomogeneous GAG distribution (black for G), while blue lines represent models with a homogeneous distribution in GAG (blue for HG). Solid lines represent models with an inhomogeneous distribution in fiber angles, while dashed lines represent models with a homogeneous distribution in fiber angles. Circles represent models with an inhomogeneous distribution in fiber stiffness, while triangles represent models with a homogeneous distribution in fiber stiffness

vs. cylindrical shape) likely contributed to differences in residual strains in the posterior AF (Duclos and Michalek 2017). Finally, our current model did not include the NP, cartilage endplate, and bony endplate, which will alter tissue swelling, and, therefore, the formation of residual stresses/strains and fiber reorientation of the full intact motion segment. Future work will investigate the effect of hydration on strain distributions throughout the disk joint.

In conclusion, the annular ring structure greatly impacts tissue swelling of thick-walled structures (e.g., 20 layer model vs. <4 layers). Development of swelling-based residual stretch in the AF was region dependent and comparable to experimental data, suggesting an important role of water absorption and swelling in stress homeostasis. Model simulations also suggest that GAG remodeling in the inner AF, due to a decrease in intradiscal pressure from the NP, likely acts to balance stress distributions throughout the AF. Lastly, findings from this study demonstrate the need to recapitulate native fiber architecture and matrix swelling behavior, as these properties will affect sub-failure and failure mechanics predicted by computational models as well as the mechanical behavior of engineered disks.

Authors' contribution Bo Yang and Grace D. O'Connell participated in study design, data analysis, data interpretation, and manuscript writing. Bo Yang did all the simulations. Both authors provided final approval for publication.

Funding This work was supported by the Signatures Innovation Fellowship from the University of California.

Compliance with ethical standards

Conflict of interest The authors declare that they have no conflict of interest.

References

Acaroglu ER, Iatridis JC, Setton LA, Foster RJ, Mow VC, Weidenbaum M (1995) Degeneration and aging affect the tensile behavior of human lumbar anulus fibrosus. Spine 20:2690–2701

Adams MA, Roughley PJ (2006) What is intervertebral disc degeneration, and what causes it? Spine 31:2151–2161

Amiel D, Frank C, Harwood F, Fronek J, Akeson W (1983) Tendons and ligaments: a morphological and biochemical comparison. J Orthop Res 1:257–265

Antoniou J et al (1996) The human lumbar intervertebral disc: evidence for changes in the biosynthesis and denaturation of the extracellular matrix with growth, maturation, ageing, and degeneration. J Clin Investig 98:996–1003

Ateshian GA, Chahine NO, Basalo IM, Hung CT (2004) The correspondence between equilibrium biphasic and triphasic material properties in mixture models of articular cartilage. J Biomech 37:391–400

Ateshian GA, Costa KD, Azeloglu EU, Morrison B, Hung CT (2009) Continuum modeling of biological tissue growth by cell division, and alteration of intracellular osmolytes and extracellular fixed charge density. J Biomech Eng 131:101001

Azeloglu EU, Albro MB, Thimmappa VA, Ateshian GA, Costa KD (2008) Heterogeneous transmural proteoglycan distribution provides a mechanism for regulating residual stresses in the aorta American Journal of Physiology-Heart and Circulatory. Physiology 294:H1197–H1205

Bezci SE, O'connell GD (2018) Osmotic pressure alters time-dependent recovery behavior of the intervertebral disc. Spine 43:E334–E340

Bezci SE, Nandy A, O'Connell GD (2015) Effect of hydration on healthy intervertebral disk mechanical stiffness. J Biomech Eng 137:101007

Botsford D, Esses S, Ogilvie-Harris D (1994) vivo diurnal variation in intervertebral disc volume and morphology. Spine 19:935–940

Bowles RD, Williams RM, Zipfel WR, Bonassar LJ (2010) Self-assembly of aligned tissue-engineered annulus fibrosus and

intervertebral disc composite via collagen gel contraction. Tissue Eng Part A 16:1339–1348
Cassidy J, Hiltner A, Baer E (1989) Hierarchical structure of the intervertebral disc. Connect Tissue Res 23:75–88
Chuong C-J, Fung Y-C (1986) Residual stress in arteries. In: Schmid-Schönbein GW, Woo SLY, Zweifach BW (eds) Frontiers in biomechanics. Springer, New York, NY, pp 117–129
Cortes DH, Jacobs NT, DeLucca JF, Elliott DM (2014) Elastic, permeability and swelling properties of human intervertebral disc tissues: a benchmark for tissue engineering. J Biomech 47:2088–2094
Demirkoparan H, Pence TJ (2018) Swelling–twist interaction in fiber-reinforced hyperelastic materials: the example of azimuthal shear. J Eng Math 109:63–84
Duclos SE, Michalek AJ (2017) Residual strains in the intervertebral disc annulus fibrosus suggest complex tissue remodeling in response to in vivo loading. J Mech Behav Biomed Mater 68:232–238
Ebara S, Iatridis JC, Setton LA, Foster RJ, Mow VC, Weidenbaum M (1996) Tensile properties of nondegenerate human lumbar anulus fibrosus. Spine 21:452–461
Emanuel KS, van der Veen AJ, Rustenburg CM, Smit TH, Kingma I (2018) Osmosis and viscoelasticity both contribute to time-dependent behaviour of the intervertebral disc under compressive load: a caprine in vitro study. J Biomech 70:10–15
Eyre DR, Muir H (1976) Types I and II collagens in intervertebral disc. Interchanging radial distributions in annulus fibrosus. Biochem J 157:267–270
Fung Y (1991) What are the residual stresses doing in our blood vessels? Ann Biomed Eng 19:237–249
Guerin HAL, Elliott DM (2006) Degeneration affects the fiber reorientation of human annulus fibrosus under tensile load. J Biomech 39:1410–1418
Gullbrand SE et al (2018) Towards the scale up of tissue engineered intervertebral discs for clinical application. Acta Biomater 70:154–164
Holzapfel GA, Schulze-Bauer C, Feigl G, Regitnig P (2005) Single lamellar mechanics of the human lumbar anulus fibrosus. Biomech Model Mechanobiol 3:125–140
Jackson AR, Yuan T-Y, Huang C-Y, Gu WY (2009) A conductivity approach to measuring fixed charge density in intervertebral disc tissue. Ann Biomed Eng 37:2566–2573
Jacobs NT, Cortes DH, Peloquin JM, Vresilovic EJ, Elliott DM (2014) Validation and application of an intervertebral disc finite element model utilizing independently constructed tissue-level constitutive formulations that are nonlinear, anisotropic, and time-dependent. J Biomech 47:2540–2546
Lai WM, Hou J, Mow VC (1991) A triphasic theory for the swelling and deformation behaviors of articular cartilage. J Biomech Eng 113:245–258
Maas SA, Ellis BJ, Ateshian GA, Weiss JA (2012) FEBio: finite elements for biomechanics. J Biomech Eng 134:011005
Marchand F, Ahmed AM (1990) Investigation of the laminate structure of lumbar disc anulus fibrosus. Spine 15:402–410
Martin J et al (2017) In vitro maturation and in vivo integration and function of an engineered cell-seeded disc-like angle ply structure (DAPS) for total disc arthroplasty. Sci Rep 7:15765
Mengoni M, Kayode O, Sikora SN, Zapata-Cornelio FY, Gregory DE, Wilcox RK (2017) Annulus fibrosus functional extrafibrillar and fibrous mechanical behaviour: experimental and computational characterisation. R Soc Open Sci 4:170807
Michalek A, Gardner-Morse M, Iatridis J (2012) Large residual strains are present in the intervertebral disc annulus fibrosus in the unloaded state. J Biomech 45:1227–1231
Nerurkar NL, Sen S, Huang AH, Elliott DM, Mauck RL (2010) Engineered disc-like angle-ply structures for intervertebral disc replacement. Spine 35:867
O'connell GD, Vresilovic EJ, Elliott DM (2007) Comparison of animals used in disc research to human lumbar disc geometry. Spine 32:328–333
O'Connell GD, Guerin HL, Elliott DM (2009) Theoretical and uniaxial experimental evaluation of human annulus fibrosus degeneration. J Biomech Eng 131:111007
Peloquin JM, Yoder JH, Jacobs NT, Moon SM, Wright AC, Vresilovic EJ, Elliott DM (2014) Human L3L4 intervertebral disc mean 3D shape, modes of variation, and their relationship to degeneration. J Biomech 47:2452–2459
Rachev A, Greenwald S (2003) Residual strains in conduit arteries. J Biomech 36:661–670
Rigozzi S, Müller R, Snedeker JG (2009) Local strain measurement reveals a varied regional dependence of tensile tendon mechanics on glycosaminoglycan content. J Biomech 42:1547–1552
Roccabianca S, Ateshian GA, Humphrey JD (2014) Biomechanical roles of medial pooling of glycosaminoglycans in thoracic aortic dissection. Biomech Model Mechanobiol 13:13–25
Rohlmann A, Zander T, Schmidt H, Wilke H-J, Bergmann G (2006) Analysis of the influence of disc degeneration on the mechanical behaviour of a lumbar motion segment using the finite element method. J Biomech 39:2484–2490
Roughley P, Hoemann C, DesRosiers E, Mwale F, Antoniou J, Alini M (2006) The potential of chitosan-based gels containing intervertebral disc cells for nucleus pulposus supplementation. Biomaterials 27:388–396
Schmidt H, Kettler A, Rohlmann A, Claes L, Wilke H-J (2007) The risk of disc prolapses with complex loading in different degrees of disc degeneration–a finite element analysis. Clin Biomech 22:988–998
Screen HR, Chhaya VH, Greenwald SE, Bader DL, Lee DA, Shelton JC (2006) The influence of swelling and matrix degradation on the microstructural integrity of tendon. Acta Biomater 2:505–513
Shirazi-Adl A, Ahmed AM, Shrivastava SC (1986) Mechanical response of a lumbar motion segment in axial torque alone and combined with compression. Spine 11:914–927
Skaggs D, Weidenbaum M, Iatridis JC, Ratcliffe A, Mow VC (1994) Regional variation in tensile properties and biochemical composition of the human lumbar anulus fibrosus. Spine 19:1310–1319
Stadie WC, Sunderman FW (1931) The osmotic coefficient of sodium in sodium hemoglobinate and of sodium chloride in hemoglobin solution. J Biol Chem 91:227–241
Urban J, Maroudas A (1979) The measurement of fixed charged density in the intervertebral disc. Biochimica et Biophysica Acta (BBA)-Gen Subj 586:166–178
Vergroesen P-PA, van der Veen AJ, Emanuel KS, van Dieën JH, Smit TH (2016) The poro-elastic behaviour of the intervertebral disc: a new perspective on diurnal fluid flow. J Biomech 49:857–863
Yang B, O'Connell GD (2017) Effect of collagen fibre orientation on intervertebral disc torsion mechanics. Biomech Model Mechanobiol 16:2005–2015
Yang B, O'Connell GD (2018) Swelling of fiber-reinforced soft tissues is affected by fiber orientation, fiber stiffness, and lamella structure. J Mech Behav Biomed Mater 82:320–328
Yasuda H, Lamaze C, Ikenberry L (1968) Permeability of solutes through hydrated polymer membranes. Part I. Diffusion of sodium chloride. Macromol Chem Phys 118:19–35
Żak M, Pezowicz C (2016) Analysis of the impact of the course of hydration on the mechanical properties of the annulus fibrosus of the intervertebral disc. Eur Spine J 25:2681–2690